Carbon 173 (2021) 433–447

Contents lists available at ScienceDirect

Carbon

journal homepage: www.elsevier.com/locate/carbon

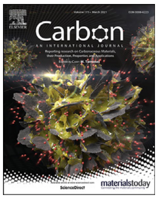

Research Article

A deep investigation into the structure of carbon dots

Keenan J. Mintz [a], Mattia Bartoli [b], Massimo Rovere [b], Yiqun Zhou [a],
Sajini D. Hettiarachchi [a], Suraj Paudyal [a], Jiuyan Chen [a], Justin B. Domena [a],
Piumi Y. Liyanage [a], Rachel Sampson [a], Durga Khadka [c], Raja R. Pandey [d],
Sunxiang Huang [c], Charles C. Chusuei [d], Alberto Tagliaferro [b], Roger M. Leblanc [a, *]

[a] Department of Chemistry, University of Miami, Coral Gables, FL, 33146, USA
[b] Department of Applied Science and Technology, Politecnico di Torino, Italy
[c] Department of Physics, University of Miami, Coral Gables, FL, 33146, USA
[d] Department of Chemistry, Middle Tennessee State University, Murfreesboro, TN, 37132, USA

ARTICLE INFO

Article history:
Received 15 September 2020
Received in revised form
3 November 2020
Accepted 6 November 2020
Available online 11 November 2020

Keywords:
Carbon dots
Nanoparticle characterization
Spectroscopy
Structure determination
Crystallography

ABSTRACT

Since their discovery, carbon dots (CDs) have been a promising nanomaterial in a variety of fields including nanomedicine. Despite their potential in this area, there are many obstacles to overcome for CDs to be approved for biomedical use. One major hindrance to CDs' approval is related to their poorly defined structure. Herein a structural study of CDs is presented in order to rectify this shortcoming. The properties of three CDs which have significant promise in biomedical applications, black CDs (B-CDs), carbon nitride dots (CNDs), and yellow CDs (Y-CDs), are compared in order to develop a coherent structural model for each nanosystem. Absorption coefficients were measured for each system and this data gave insight on the level of disorder in each system. Furthermore, extensive structural characterization has been performed in order to derive structural information for each system. This data showed that B-CDs and CNDs are functionalized to a greater degree and are also more disordered and amorphous than Y-CDs. These techniques were used to develop a structural model consistent with the obtained data and what is known for carbonic nanostructures. These models can be used to analyze CD emission properties and to better understand the structure-property relationship in CDs.

1. Introduction

Carbon dots (CDs) are a class of carbon-based nanoparticles discovered in the early 21st century [1–3]. Since then they have been researched in many fields and they appear to be a promising material for different applications, including drug delivery, photocatalysis, bioimaging, and sensing [4–7]. Despite the advances in the potential applications of CDs, their fundamental properties have remained points of uncertainty and debate [8–10]. This lack of clarity has inhibited the ability of researchers to systematically improve the properties of CDs since the structural and electronic properties are poorly defined and the relationship between the two is even less clear. Additionally, this confusion hinders the ability of CDs to be used in some applications, as it is unlikely that they will be approved for biomedical use in humans without a clearly defined structure [11]. For these reasons it is imperative to seek insight on this topic.

Due to the wide variety of literature related to CDs, there is also diverse and somewhat confusing terminology in this area. CDs may be referred to as carbon quantum dots, carbon nanodots, carbon nanoparticles and more [12]. The particles in this work may be referred to as CDs or carbon nanodots. Since there is no evidence that quantum confinement plays a role in the PL mechanism for these CDs, carbon quantum dots would not be accurate, and carbon nanoparticles is a more general term which does not provide much information regarding our particles. Similarly to the issues with nomenclature, there are many hypothesized structures for CDs which have been reviewed on a few occasions [9,13,14]. The fact that there are varying interpretations of structural data is hardly surprising as there are countless precursor and reaction method combinations published in the current literature. One would expect divergent hypotheses, especially for different CDs made from top-down versus bottom-up approaches. Additionally, there is a distribution of sizes found among all CDs, indicating that there are

---

* Corresponding author.
E-mail address: rml@miami.edu (R.M. Leblanc).

https://doi.org/10.1016/j.carbon.2020.11.017

differences, at the very least, in the size of the structures found in a single CDs preparation. These considerations must be considered when relating data to CD structure.

Many researchers have proposed a graphitic-like core, either amorphous or crystalline [15–18]. Others have suggested an amorphous core of pure sp^3 carbon or a ratio of sp^3:sp^2 carbon [19,20]. The role of heteroatom doping has been explored in CDs, not just for surface structure, but also hypothesized in the core [21,22]. Some organic functional groups are also believed to be in the core, such as carbonyls or various types of nitrogen-containing groups [23–25]. For all of these examples, evidence is provided for the presence of the appropriate group or structural motif, but there is yet to be a strong structural model for CDs [26]. Additionally, the physical and electronic connection is often not discussed beyond generalizations regarding electron transfer [27,28]. In this paper, we endeavor to remedy this shortcoming for three CDs preparations in our lab (Fig. 1).

Black CDs (B-CDs) are prepared through a top-down method involving acidic oxidation and were first reported in 2015 [29]. Since then B-CDs have shown to be a promising material for bone-specific drug delivery, delivery across the blood-brain barrier (BBB), or cell-membrane penetration with an attached targeting ligand [24,30]. Carbon nitride dots (CNDs) are prepared from a bottom-up microwave-mediated approach and have shown ability to selectively target glioblastoma cells and self-target the BBB for drug delivery [31,32]. Finally, yellow CDs (Y-CDs) are prepared through a bottom-up ultrasonication method which have been used in 3D printing, demonstrated ability in inhibiting β-amyloid fibril formation, and been able to permeate the entire body of zebrafish, including the central nervous system [33,34]. Based on our previous work cited here these have been shown non-toxic in several *in vitro* and *in vivo* models (several cellular models, sea urchin embryos, and zebrafish [30–32,34,35]. These three represent diverse precursors, methods, and resulting properties, yet all fall under the same class of material (Fig. 1). To better understand these systems, and CDs in general, and also to enable their potential use in biomedical applications in the future, we embarked on this study to develop a structural model for each of them using the current techniques available.

The challenges with analyzing data related to CD structure are multiple, but two will be mentioned briefly. First, as previously mentioned there is a size distribution related to CDs indicating a potential distribution of structures in each CDs sample. Even for tediously separated CDs systems there remains a range of sizes and optical properties [36,37]. This complicates structural data interpretation for these systems. Secondly, for many techniques, it is not immediately apparent if the recorded signals are coming from the core or surface of CDs. Fourier transform infrared (FTIR), X-ray photoelectron (XPS), electron spin resonance (ESR), and Raman spectroscopies are all capable of penetrating 10 nm or more (the commonly defined maximum size for CDs), and so it must be inferred, if possible, where the signal from these techniques is coming from. Thermogravimetric analysis (TGA) also possesses interpretational ambiguity when there are more than two peaks as they cannot be simply assigned to surface and core depending on the temperature of decomposition. Zeta potential can provide surface information, but it is related to surface charge and provides little detail. Nuclear magnetic resonance (NMR) can potentially give surface information exclusively, depending on the composition of the core [38]. X-ray techniques such as X-ray diffraction (XRD) should provide only core information, as it is looking at lattice spacings which would not be present on the surface of the particle. Intraparticle interactions may be a small contribution to this technique, but the signal would assuredly be minor compared to core lattices.

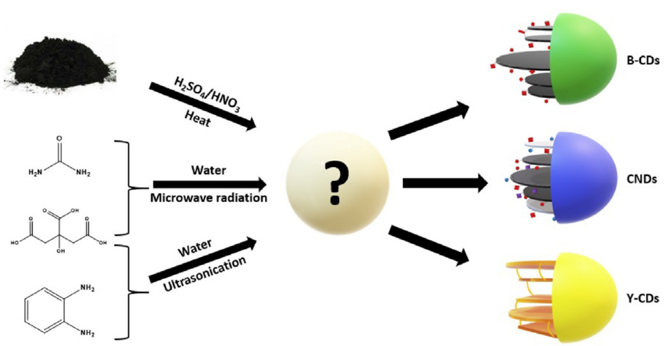

Fig. 1. Representation of three different preparation methods and the resulting structures. (A colour version of this figure can be viewed online.)

In this work, the optical properties of the previously reported CDs have been compared and deeply analyzed. The analysis of CD absorption coefficients relation to excitation energy has been reported for the first time to the best of our knowledge. Furthermore, the abovementioned structural characterization techniques were performed on our CD systems to examine their structural properties. Finally, this data was combined to develop coherent models for the structure of each CD.

2. Materials and methods

2.1. Materials

Carbon nanopowder (<100 nm) and 1,2-phenylenediamine flakes (99.5%) were procured from Sigma-Aldrich (St. Louis, MO). Anhydrous citric acid (BDH) was obtained from VWR (West Chester, PA). Urea was acquired from Eastman Kodak Company (Rochester, NY). Sulfuric acid (98%) and nitric acid (68–70%) with ACS grade were purchased from ARISTAR (distributed by VWR, Radnor, PA). Compressed argon with ultrahigh purity was secured from Airgas (Miami, FL). Chloroform was obtained from MP Biomedicals (Irvine, CA) Dialysis tubing with molecular weight cutoff (MWCO) of 3500 was bought from Thermo Scientific (Rockford, IL). Dialysis tubing with 100–500 Da MWCO was obtained from Spectrum Labs Inc., (Rancho Dominguez, CA). The size exclusion chromatography (SEC) was performed using GE Healthcare Sephacryl S-300 (Uppsala, Sweden) as the stationary phase. Deionized (DI) water used was ultrapure (type I) water which was purified using a Millipore Direct-Q 3 water purification system acquired from EMD Millipore Corp. The purified water displayed a surface tension of 72.6 mN m^{-1}, a resistivity of 18.2 MΩ cm and a pH value of 7.0 ± 0.3 at 20.0 ± 0.5 °C. All the chemicals were used as received.

2.2. Instrumentation

UV–vis spectra were obtained from an Agilent Cary 100 UV–vis spectrophotometer. Photoluminescence (PL) characterization were performed on a Fluorolog HORIBA Jobin Yvon fluorometer with a slit width of 5 nm for excitation and emission. All optical characterization spectra were obtained with quartz cells possessing a pathlength of 1 cm. The attenuated total reflection infrared (ATR-FTIR) spectra were obtained from a FTIR spectrometer (FT-Nicolet 5700, Thermoscientific) equipped with a Smartorbit (Thermoscientific) operating in attenuated total reflectance (ATR) in a range between 600 cm^{-1} to 4000 cm_{-1}. The Zeta potential was recorded on a Malvern Zetasizer nano-series.

XPS spectra were taken using a PerkinElmer PHI 560 system with a double-pass cylindrical mirror analyzer operated using a Mg

Kα anode with a hν = 1253.6 eV photon energy at 13 kV and 250 Watts. CD samples were mounted as a powder onto the sample holder using a conductive double-sided tape (Ted Pella, Inc.; Redding, CA, USA). NMR data was obtained from a Bruker 300 MHz NEO nanobay instrument with D_2O as solvent.

Raman spectra were recorded using a Renishaw Inviah Spectrometer equipped with a blue (457 nm), green (514.5 nm), and red (wavelength 785 nm) laser source and a 50x objective. Applied power using green laser source was in the range of 10–100 μW, with the red laser line from 50 to 500 μW and for the blue laser line from 100 μW to 1 mW. B-CDs were sampled in three different points while only one reliable signal was acquired for CNDs due to the strong fluorescence of the powder. Y-CDs were measured in three different points.

ESR measurements have been performed using a Brucker EMXNano bench instrument. Feeding a variable microwave power (ranging from 1 μW to 100 mW) to the cavity filled with the samples and sweeping the applied magnetic field from 3360 G to 3560 G the ESR signal was recorded. A marker was inserted in the resonant cavity and measured at the same time as the samples in order to allow the precise evaluation of the g-value and of the relative spin density. The measured signal was also fitted using derivatives of lorentzian and gaussian function to have a better evaluation of the area of the ESR signal for each sample and more accurate value for their centers. TGA of each type of CDs was performed using a Netzsch TG 209 F3 Tarsus thermo-microbalance while heating under a nitrogen flow from 40 to 1000 °C at a rate of 10 °C/min.

XRD patterns were collected with a Phillips X'pert Diffractometer that uses a copper source (0.154 nm wavelength). The lattice spacing d can be calculated from the Braggs condition: $2d\sin\theta = n\lambda$, where 2θ is the peak position in the XRD pattern. Small angle X-ray scattering (SAXS) was performed with a GeniX 3D microfocus Cu Kα source (0.154 nm wavelength) with 3 sets of 4-blade slits for scatterless collimation. Wide-angle (WAXS) detection was enabled through a Hybrid Pixel Array Pilatus detector by Dectris. Kapton tape was used to fix the sample in place and the resulting pattern of the CDs was compared to the background of the tape alone.

2.3. Preparation of B-CDs

The preparation and purification of each sample has been previously reported but will be restated in brief for clarity. 1 g of carbon nanopowder was mixed with 36 mL of concentrated H_2SO_4 and 12 mL of concentrated HNO_3. This mixture was refluxed at 110 °C for 15 h. After the reaction, the mixture was cooled down to room temperature and then neutralized with a saturated NaOH solution in an ice bath and then vacuum filtered repeatedly to remove unreacted carbon powder. The solution was then placed in an ice bath to crystalize salts (sodium sulfate or nitrate) from the saturated solution, seeding with Na_2SO_4 as needed, and vacuum filtered to remove the salts. This process was repeated multiple times. The purified solution was transferred to a separatory funnel and washed 3 times with 15 mL of chloroform to remove organic impurities. The aqueous solution was then centrifuged for 30 min at 3000 rpm and the supernatant was transferred to a dialysis bag (MWCO 3500 Da) for 5 days, changing the DI water every 4–10 h. After dialysis, the water was removed by a rotary evaporator to obtain B-CDs powder.

2.4. Preparation of CNDs

Citric acid (0.5 g) and urea (0.5 g) were mixed in 25 mL DI water and stirred vigorously overnight. The mixture was then placed into a domestic microwave oven and heated at 700 W for 7 min. The resulting black solid was dispersed in 15 mL DI water and sonicated for 30 min at 42 kHz. This solution was centrifuged twice for 15 min at 1500 rpm. The supernatant was filtered with a 0.2 μm cellulose syringe filter and then transferred to a dialysis bag (MWCO 100–500 Da) and dialyzed against DI water for 3 days changing the water every 24 h. The water was then removed with a rotary evaporator to obtain CNDs powder.

2.5. Preparation of Y-CDs

To prepare Y-CDs, 0.56 g of *o*-phenylenediamine (*o*-PDA) was mixed with 0.04 g of citric acid in 10 mL of DI water and sonicated under argon gas for 1 h at 42 kHz. The solution color was orange after the reaction and the mixture was cooled in an ice bath to remove unreacted *o*-PDA. The mass of unreacted *o*-PDA was 0.127 g indicating 0.433 g reacted which creates an effective molar ratio between citric acid and *o*-PDA of 1:19. The CDs were then purified with SEC using Sephacryl S-300 as the stationary phase and DI water as the mobile phase. After SEC, the water was removed through lyophilization to obtain Y-CDs powder.

3. Results and discussion

3.1. Basic CDs characterization

All CDs analyzed in this study have been previously reported [29,31,33]. Traditional characterization methods for CDs were reexamined to highlight the similarities and differences among the different systems and to relate these previously reported properties with the main current structural investigation.

3.1.1. Optical properties

We will begin this comparison with the UV–vis absorption properties of the three CDs (B-CDs, CNDs, and Y-CDs). There is some difference between the exact peak positions however all three CDs possess absorption peaks in the 200–300 nm region (Fig. 2A, Table S1) This is unsurprising as many carbonic structures show absorbance in this region commonly attributed to the π-π* transition of the C=C bond and sp^2 networks as in graphene [8,26,39]. The peaks between 300 and 400 nm are usually ascribed to the n-π* transition of the C=O or C=N bond although this is attributed to peaks below 300 nm in some cases [33]. It is interesting to note that Y-CDs do not possess much discernible absorption in this region indicating the first difference between the CDs. This difference continues with the presence of a peak above 400 nm for Y-CDs which is not present for B-CDs or CNDs. This is believed to be due to the formation of $-NO_2$ group by the oxidation of the $-NH_2$ group during the preparation process [40,41]. These differences will be revisited when discussing the functional groups detected through FTIR and XPS. There is one more difference which can be observed from the comparison of absorption spectra (Fig. 2a). A low energy tailing is observed for the B-CDs and CNDs spectra, but much less so for Y-CDs. This data can provide information about the π electronic bands in a nanostructure and the degree of order in a system [42,43]. To obtain this information the absorption coefficient (α) must first be measured at a range of energies. To do this, the extinction coefficient was calculated by taking the absorption spectra of several concentrations of CDs (Fig. S1) and plotting the absorbance vs. concentration in 10 nm increments across the tailing region of the UV–vis spectra. The slope of these plots was taken as k, and α was calculated according to Equation S1. The ln(α) was plotted vs. excitation energy and data sets was fit with parabolic functions (Fig. 3). This relationship can be described by Equation S(2) and depends on σ which is a gaussian parameter describing the width of the π band and can be correlated with the order/

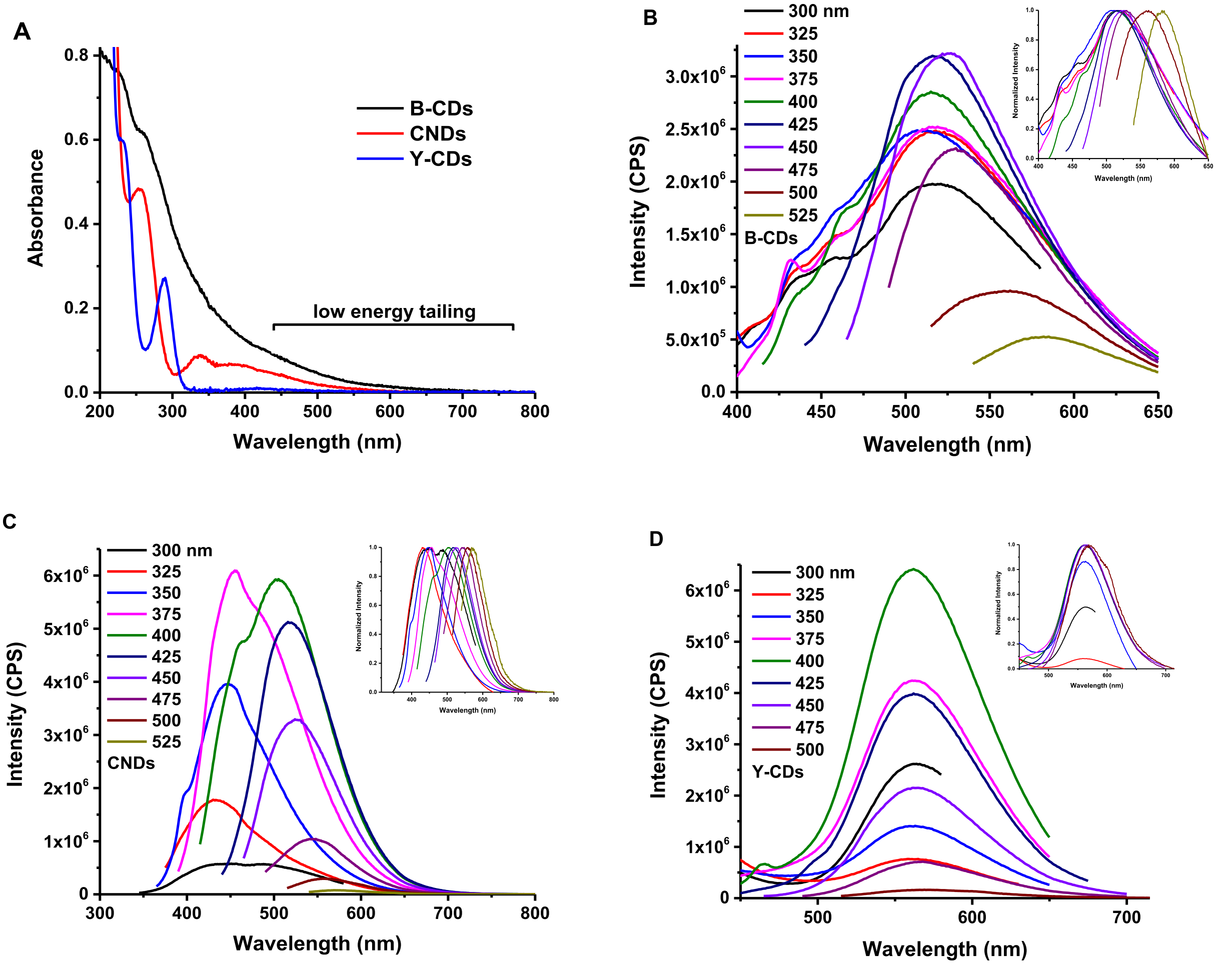

Fig. 2. UV–vis absorbance spectra (A) and PL spectra for B-CDs (B), CNDs (C), and Y-CDs (D). Optical pathlength was 1 cm for each measurement and the solvent was deionized water. (A colour version of this figure can be viewed online.)

disorder of a system [44]. This value can be extracted from the parabolic function according to Equation S(3) and the values for each sample are reported in Table 1. A higher value for σ indicates a greater degree of disorder so B-CDs should have the most disordered structure. The plot for CNDs in Fig. 3 clearly shows two regions of contribution and are fitted to separate functions. The region at higher energy displays more order, similar to Y-CDs, compared to the lower energy contribution. The presence of two regions for CNDs indicates the existence of distinct molecular-like clusters with differing degrees of order. In terms of overall order, the trend is B-CDs, CNDs, Y-CDs in terms of increasing order. This will be discussed in further detail in correlation with ESR data in section 3.2.

The PL spectra of each CDs shown in Fig. 2 shows quite disparate properties. Although the maximum excitation for each species are within 50 nm of each other, the maximum emission wavelength ranges from 450 nm (CNDs) to 565 nm (Y-CDs) with B-CDs possessing an emission maximum of 520 nm. This wide emission range displays the diversity which is found among CDs and indicates

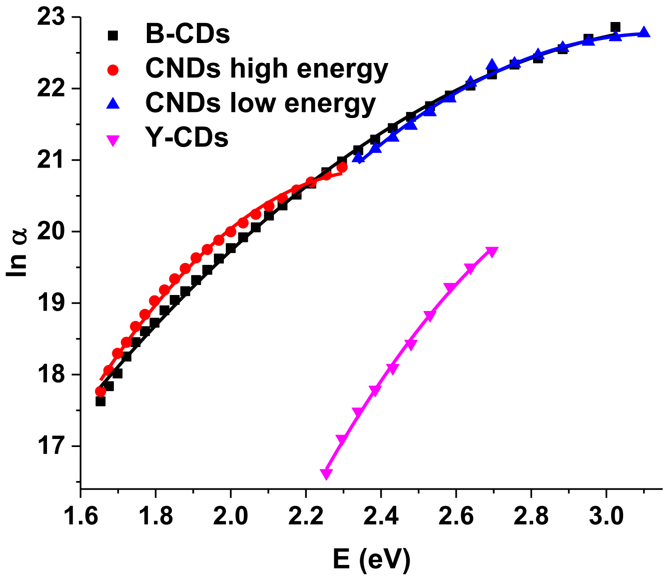

Fig. 3. Plot of ln α vs. energy for various CDs. The fitted curves are parabolic and the lowest R^2 value is 0.993. (A colour version of this figure can be viewed online.)

Table 1
σ values extracted from the parabolic functions in Fig. 2.

Sample	σ (eV)
B-CDs	0.37
CNDs high energy	0.21
CNDs low energy	0.30
Y-CDs	0.22

potentially a significantly different structural origin. This is highlighted further by the fact that B-CDs and CNDs possess excitation-dependent emission while Y-CDs do not. Excitation-dependent emission is perhaps the most interesting and debated property of CDs and the comparison of particles possessing this property with those that do not should help to shed light on the origin of this phenomenon. Since B-CDs and CNDs possess excitation-dependent emission their Stokes shift depends on the excitation wavelength, so for direct comparison, Stokes shift was calculated using the maximum excitation wavelength (Table S1). B-CDs and CNDs possess an approximate shift of 90 nm which is quite large compared to organic fluorophores, but Y-CDs' Stokes shift is much higher at 165 nm [45]. A large value for Stokes shift indicates significant non-radiative relaxation from higher energy levels prior to the release of a photon from an emissive energy level [45,46].

Another feature which is more common for CDs than organic fluorophores is broad emission peaks [26,47]. The full width at half maximum (FWHM) for these CDs is no exception (Table S1). B-CDs and Y-CDs possess FWHMs of close to 100 nm while CNDs' is larger at 130 nm. The broader emission peaks could be related to a greater number of vibrational energy levels in the ground state than typically found for other fluorescent species. This large FWHM for CNDs also contributes to the higher quantum yield (QY) found in this system (12.5%, Table S1). The QY was calculated for these species using the standard reference method with Equation S4, which uses the integrated area of the PL curve. An increased FWHM would provide a larger value for this area compared to a smaller FWHM. The increased area under the PL curve for CNDs helps to dramatically raise the QY over B-CDs and Y-CDs (~1%), but this certainly does not account for the entirety of the difference. Nitrogen doping is thought to dramatically increase QY for CDs, although the mechanism behind that phenomenon is not always clear [48].

For deeper PL analysis, in Fig. S2 we report Raman peaks as black squares which can be fitted using a straight line. As the Raman shift with respect to the excitation light energy is fixed, this linear behavior is expected. The energy independent peaks were due to transitions (n-π*, π-π*) involving the electronic levels of the molecular fragments contained into CDs species. In Fig. S2A, data related to B-CDs are reported. Considering the functionalities detected previously described, the spaced transitions are due to n-π* of the several oxygen residual groups ranging from high energy (C=O) to low energy (C–O–C, C–O–H). Highest energy transition was due to n-π* of C=O quite close to the energy of graphitic π-π* gap. Y-CDs showed a different pattern due to the more complex structure. In this case, the π-π* transition due to aromatic moieties was appreciable (Fig. S2B, blue lines, 3.43 eV) similar to the π-π* transition due to nitrogen included in aromatic rings (Fig. S2B, red lines). Furthermore, plenty of n-π* transitions were appreciable (Fig. S2B, pink and green line) and they were possibly due to carboxylic systems (free functionalities and amides). Interestingly, a transition at around 2.2 eV was observed and reasonably identified as n-π* transition of free amine residue of *o*-PDA (higher n energy). A more complex pattern was observed for CNDs and is reported in Fig. S2C. In this case, n-π* were the dominant transitions and can be reasonably assignedto the high nitrogen content related to amides and aromatic nitrogen. Due to the very complex structure of CNDs, the energy associated to n-π* transitions of nitrogen related residue was affected by the small but significant differences of molecular environment causing the trend observed in the pink, green and blue lines of Fig. S2C.

The totality of CDs' literature illustrates the disparate properties which can result from this material. The CDs produced in our lab are no different. The optical properties of B-CDs, Y-CDs, and CNDs show different properties and the differences appear to be random (e.g. excitation-dependence is found in B-CDs and CNDs, yet low QY is found in B-CDs and Y-CDs). This shows the implausibility of developing a single model for all CDs preparations. These properties will need to be revisited to examine the feasibility of our proposed structures to be discussed later.

3.1.2. Size and morphology

While the optical properties discussed above display some contrast, the data obtained from atomic force (AFM) and transmission electron (TEM) microscopies are quite similar for each system (Figs. S3 and S4 and Table S1). B-CDs have a mean size of 3 nm and are slightly larger than Y-CDs (2 nm) and CNDs (2.4 nm) as determined by counting at least 100 particles from TEM images. It is interesting to note that CNDs and Y-CDs are very close in size, but their optical properties share little commonality, further indicating the need for multiple models. Based on the complementary data of AFM and TEM it appears the particles should be at least roughly spherical, which is obviously an important consideration concerning the structure of the CDs' core. A pure carbon core for CDs would present two main possibilities: a collection of 2D structures (e.g. graphitic) or a structure with 3D bonding (e.g. diamond-like). The presence of heteroatoms assuredly complicates this oversimplification, at least for Y-CDs and CNDs. While the values obtained from these techniques do not provide structural details, they provide important boundaries against which to fill the proposed structures of CDs.

3.1.3. Surface/core functionality

FTIR and XPS are commonly used as the main techniques to provide information on the groups present in CDs. The FTIR data denotes structural features within the bulk of the CDs while the signal from XPS emanates largely from the top-most (5–10 nm) surface of the CDs [49,50]. The availability on the surface may affect intensities, leading to a surface bias in determining the amount of each group or element in the particle from XPS. Due to the qualitative and more established nature of FTIR it will be discussed in this section, followed by XPS in the next section.

CNDs and Y-CDs display similar groups from FTIR (Fig. 4, Table S1) with more difference being shown with B-CDs. All particles possess a peak indicative of the –OH or –NH group, although the breadth of the peak suggests –COOH for B-CDs and CNDs. For Y-

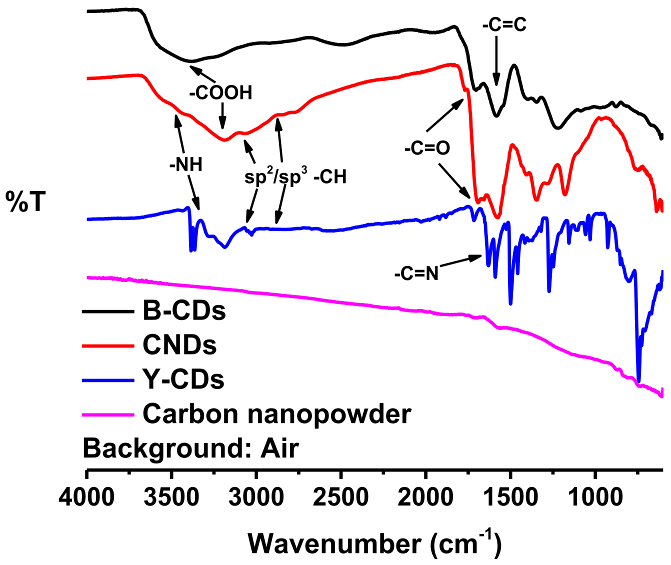

Fig. 4. FTIR spectra for B-CDs, CNDs, Y-CDs, and carbon nanopowder with main peaks for all samples highlighted. (A colour version of this figure can be viewed online.)

CDs, their spectrum (Fig. 4) shows the ν_{NH} of un-protonated species around 3300 cm^{-1} while the protonated one has a broader peak at about 3200 cm^{-1}. The ν_{CH} of aromatic moieties are visible at 3013 cm^{-1} while the ν_{CH} at 2875 and 2900 cm^{-1} could be ascribed to the saturated ν_{CH}. They also all possess −C=O bonds, which is supported by the previously discussed UV−vis spectra. B-CDs and Y-CDs show shared peaks (~1550 and 1700 cm^{-1}) indicating −C=C and -C-O bonds, while in contrast, CNDs possess the −C=N bond and aromatic carbon. These two groups (-C=N and aromatic carbon) are expected to be present in a nitride possessing structure such as CNDs. Amides were also detected with $\nu_{C=O}$ peak at 1654 cm^{-1} and similarly aromatic rings were detected with $\nu_{C=C}$ at 1595 cm^{-1}. Pyridine-like structures were responsible for $\nu_{C\text{-}N}$ at 1486 cm^{-1}. For Y-CDs, peaks which can result from $-NO_2$ groups (~1500 cm^{-1}) and from poly(phenylenediamine) (1422 and 1208 cm^{-1}) are observed. According to Olgun et al., $\nu_{C=C}$ shifts at lower wavenumbers in poly(phenylenediamine) and it is detectable at 1550 cm^{-1} instead of 1600 cm^{-1} [51]. The spectrum for B-CDs is much simpler in comparison to Y-CDs and CNDs. The FTIR spectrum of carbon nanopowder (Fig. 4) did not show any significant peak according to the low functionalization on pristine carbon surface.

The slight shifting of peaks between spectra and the realization that peaks with weak intensity can be obscured highlights the need for the more exact and quantitative technique of XPS. It should also be noted XPS is surface sensitive, and that 10 nm is the upper limit of the technique's sampling capability. It is possible for top-most, contiguous structural overlayers to attenuate photoelectrons underlying the surface. Before moving on, Zeta potential, another technique related to surface characterization, of the CDs will be discussed. B-CDs and CNDs possess a Zeta potential value around −38 mV indicating a large electrostatic repulsion between particles leading to high aqueous stability (Table S1). Despite the similarities between surface functional groups for CNDs and Y-CDs, the Zeta potentials are quite different with a value of −12.2 for Y-CDs. This shows a lower aqueous stability for Y-CDs which is supported by the dispersibility properties of Y-CDs previously reported [33]. It also suggests that B-CDs and CNDs should have much higher surface coverage of polar functional groups such as -OH, −COOH, etc. The negative Zeta potential of Y-CDs also suggests many amine groups are consumed in the reaction as the *o*-PDA is present in much higher concentration than citric acid, yet the product possesses a negative surface charge. To receive more information on the type and quantity of surface groups on the CDs, XPS was performed for all three systems.

3.2. Advanced CDs characterization

3.2.1. Surface/core functionality

The values from XPS shows much greater similarity between B-CDs and CNDs than Y-CDs (Fig. S5, Table S2). B-CDs shows 54.6% carbon (−COOH [289.7 eV] and C−C/C=C [285.9 eV]) and 43.8% oxygen (-COOH [534.0 eV] and -C-O/-C=O [532.7 eV]) [29]. This data agrees with what is seen from FTIR and provides important quantitative data which will be discussed later. CNDs values are not too dissimilar, with 43.3% carbon (-C-O [286.8 eV] and −COOH [289.7 eV]) and 48.6% oxygen (-C-O [531.9 eV]) detected, although unsurprisingly, significant amounts of nitrogen are detected (8.1%, −C=N [401.1 eV]) [31]. This is a smaller value than we would expect for the C_3N_4 carbon nitride structure and this may be due to a high density of surface groups as indicated by a high percentage of oxygen.

Y-CDs, in contrast to B-CDs and CNDs, displays a high carbon content (93.4%, −C=C [284.9 eV] and -C-O [286.8 eV]) with 5.2% oxygen (-C=O [532.6 eV] and -C-O [531.2 eV]), and 1.4% nitrogen (pyrrolidonic, [399.4 eV]). The low functionalization with oxygen is attributed to the gentle reaction conditions and lack of thermal treatment for Y-CDs which are not capable of oxidizing the surface as observed for B-CDs and CNDs. This also correlates with the lower Zeta potential and the tendency to dissolve better than the other two CDs in organic solvents [33]. The values obtained from XPS will be useful in calculations related to the CDs' composition described later in this article.

Solution state NMR was used to try to extract additional structural information (Fig. S6). NMR is a powerful tool for structure determination for organic molecules but obtaining good data for nanoparticles can be difficult. Each shows the solvent peak (D_2O) at 4.8 ppm. All CDs show a peak indicative of alkenes (~2.2 ppm) and traces of alkanes (<2 ppm) and/or aromatics (7−8 ppm). CNDs and Y-CDs also show aromatic adjacent protons with complex splitting at just less than 3 ppm. The peak at ~7 ppm in Y-CDs could be related to the amide bond from connection of citric acid and *o*-PDA. Unsurprisingly, not much detail can be obtained beyond simple assignment and solution state NMR is not sensitive enough to detect groups detected through FTIR and XPS (e.g. −COOH, −OH, etc.). Solid state NMR may produce a more complete picture of CDs but acquiring quality data from this technique for CDs would require significant run times.

A typical raw Raman spectrum is reported in Fig. S7. The rising slope on which the Raman signal is superimposed is due to PL and this background is subtracted in Fig. 5B. The signal was recorded in 3 areas and the signals were similar suggesting that the sample is reasonably uniform (Fig. S8). The peaks observed are those typical of sp^2 carbon. The decomposition of the signal in the region of the sp^2 carbon contribution (1000-2000 cm^{-1}) shows that the material is reasonably ordered and quite graphitic. This agrees with the limited amount of non-radiative recombination paths related to disorder that can hinder PL.

For CNDs, several points of the sample were analyzed as well. In all but one of them the PL background was so strong that it was not possible to see the Raman contribution, which corresponds with the high QY discussed previously. In one point, however, the Raman contribution was evident. The PL subtracted spectrum for this point is reported in Fig. 5C. In addition to the typical peaks of sp^2 carbon an additional one can be observed close to 2200 cm^{-1} that can be assigned to CN bonding (triple bond). The sp^2 carbon signal can be deconvoluted in the usual D and G contributions and it appears that D band is much larger than in the previous case indicating that in

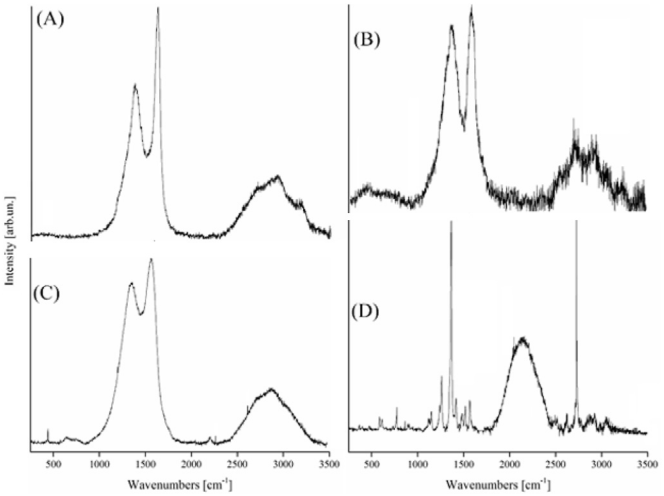

Fig. 5. Raman spectrum for carbon nanopowder (A), B-CDs (B), CNDs (C), and Y-CDs (D).

the sample point in which the PL background is lower the material is more disordered than in B-CDs and indicates the presence of polyaromatics. The spectra are plotted together in Fig. S8 and this highlights the difference between these two samples. CNDs are more disordered (enlarged D and G peaks, limited depth of the valley between D and G peaks) while B-CDs' spectrum indicates a higher degree of order in the structure. The disordered structure may lead to the lower PL background which enables the observation of the Raman spectra. The strong PL background observed in other points is consistent with an ordered structure, so the overall order of CNDs' structure may be higher than B-CDs despite the Raman spectra. Both Raman spectra are compatible with the thermal evolution of the Raman spectra of a carbonized polyaniline [52].

The Raman spectra recorded for Y-CDs displayed marked differences (Fig. 5D). These were recorded in several points showing reasonable uniformity of the sample as the same set of peaks (albeit with different relative intensities) is found in all spectra. The peaks are quite narrow and overall, the spectra are quite different from those of the two previous samples. Most probably organic molecules (or more in general oxyhydrogenated carbon compounds) are present in addition to sp^2 carbon, and the structures are smaller and more ordered than for the two other samples. The peak at 1366 cm^{-1} can be attributed to the carbon D-peak and that at 2725 cm^{-1} to its 2D replica. The fact that the D-peak is narrow points towards a rather ordered local structure, keeping in mind that the D-peak is not related to disorder but indirectly to the size of the sp^2 coordinated ring domains. The presence of the D peak suggests that a G-peak should also be present. The most probable candidate is the peak at 1518 cm^{-1}, that will also give rise to D + G and 2G peaks at 2870 and 3052 cm^{-1}, respectively. These Raman spectra for Y-CDs indicate a uniform material and the narrowness of the peak points towards an ordered structure. The set of peaks observed between 1000 and 1600 cm^{-1} is compatible with the Raman spectra of diphenylamine and phenazine [53,54].

The carbon nanopowder (B-CDs' precursor) were sampled in two different points using all three-laser lines. At a visual inspection with the optical microscope the material appears like a medium grained carbon powder. We measured a typical signal of carbon-based material using the green line with different degrees of fluorescence while on the red and blue line the fluorescence was the main characteristic with more or less evident traces of G-peak on the red and blue lines (Fig. 5A and S9). This material shows an amorphous carbon-based material behavior with different degree of disorder from point to point, a slight variation of D peak width that appear to be right shouldered in one sample. 2D region is typical of an amorphous material with evident remnants of 2D, D + G, 2G peaks. Using the red laser line, we observe the shift of the peak of fluorescence to lower Raman shift around the region 500 to 1500 cm^{-1}. Using the blue laser line, we observe a strong fluorescence signal with traces of the G peak around 1600 cm^{-1} (Fig. S9). As mentioned above, the small signals observed do not allow a quantitative analysis of the peak. The Raman signal is similar to that of glassy carbon although the G-peak appears more intense than in glassy carbon spectra indicating this sample may possess a more graphitic nature [55].

ESR measurements were performed on each CDs sample and carbon nanopowder as well. From the linewidth of the signal and the intensity of the signal with respect to the square root of the microwave power it is possible to extract information about the values of the spin-lattice (T_1) and spin-spin (T_2) relaxation times. Such values are reported (together with the relative amount of spin density and the g-value using the standard deviation of sample measurements as uncertainty) in Table 2 and the ESR spectra in Fig. S10.

Table 2
Summary of data derived from ESR measurements.

Sample	T_1 (μs)	T_2 (ns)	Ns (relative)	g-value
B-CDs	2.1	23.5	21	2.0040 ± 0.0004
CNDs	4.8	20	3	2.0044 ± 0.0005
Y-CDs	260	21	1	2.0043 ± 0.0003
C nanopowder	0.025	10	1056	2.0026 ± 0.0001

The g-values for B-CDs, Y-CDs, and CNDs are similar to each other and are typical of organic-like structures, which may be due to the surface functionalization. The value for carbon nanopowder indicates that it is most probably associated to electrons sitting in states belonging to sp^2 coordinated carbon atoms. It also appears that they are delocalized over a few atoms. The difference between this value and the g-value for B-CDs most likely arises from the surface oxidation generated in B-CDs during their preparation. There is also a dramatic difference in signal intensity for carbon nanopowder. Even if we take into account that the amount of material used might be different by a factor 3 to 4 at most (it is difficult to estimate the actual amount of the analyzed powder for a number of reasons) it remains that this sample has a much larger number of ESR active states compare to the three others.

Relaxation times T_1 and T_2 in Table 2 are calculated after fitting the plot of the square root of the applied microwave power on the X-axis, and the area of the ESR signal on the Y-axis for each sample. The results show that while T_2 shows minor difference among the various samples, T_1 (describing the spin-lattice interaction and usually shortened by the presence of distorted networks) varies by order of magnitudes, being large in Y-CDs, shorter for B-CDs and CNDs, and much shorter for carbon nanopowder. The presence of distortion also leads to a much higher correlation energy (i.e. the extra cost to fit a second electron in a singly occupied state). This means that a wider energy region of the density of states near Fermi level is singly occupied leading to a higher value of the spin density as well for carbon nanopowder. Raman analysis provided evidence that Y-CDs have the most ordered structure. This is supported also by the larger (by far) value of T_1 (Table 2), which indicates that the local distortions are much lower. This also agrees with the correlation between α and energy seen in Fig. 3. Y-CDs possesses the most order/least distortion with the reverse being true for B-CDs. For CNDs, the presence of two contributions complicates the analysis. Based on the σ values (Table 1) and T_1 values (Table 2), the overall order of the system is between B-CDs and Y-CDs, however the high energy contribution to the absorbance coefficient plot (Fig. 3, Table 1) shows order on the level of Y-CDs. The more organized cluster on CNDs is most likely enriched in carbon compared to the less organized structure enriched in oxygen and nitrogen. The structure with the higher level of carbon absorbs at higher energies and is more ordered, but the presence of oxygen and nitrogen shifts the optical transitions to slightly lower energies and introduces more distortions to the system. The presence of heteroatoms reduces the average coordination number of the system allowing for more distortions, thus reducing the order.

TGA was conducted on B-CDs, CNDs, and Y-CDs to discern their respective surface compositions and compare their thermal stabilities and discern their respective surface compositions. Nitrogen gas was used to avoid oxidation of the CDs during heating. Fig. 6A shows five decomposition stages of B-CDs, namely 40–173, 173–448, 448–613, 613–763, and 763–1000 °C. The initial slight mass loss of 11% before 173 °C is due to the evaporation of water molecules adsorbed by B-CDs or generated in dehydration reactions [56,57]. In comparison, when the temperature is increased from 173 to 448 °C and from 448 to 613 °C, the mass loss of B-CDs achieves up to 48%, which may result from the decomposition of

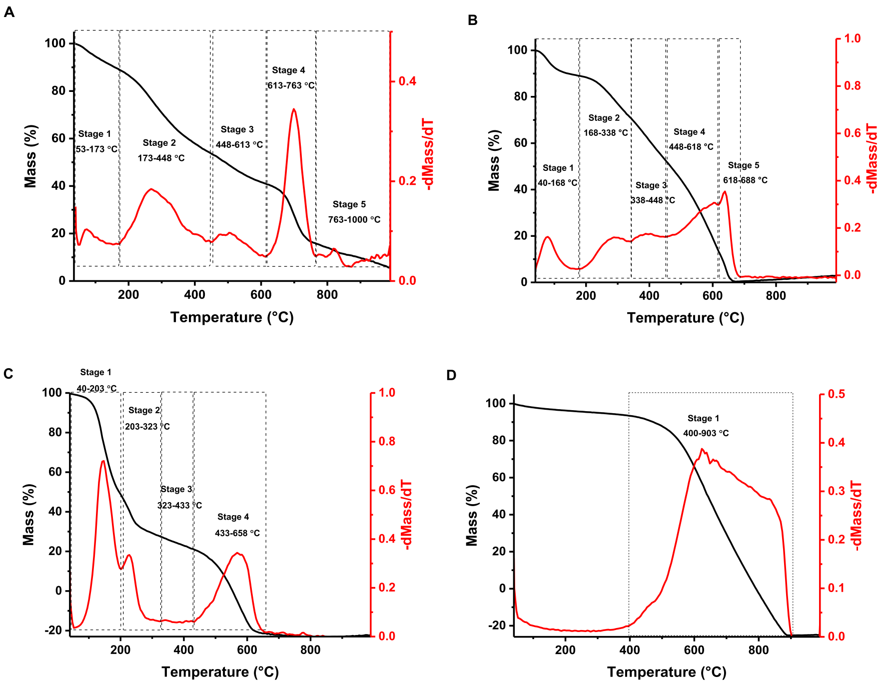

Fig. 6. Thermograms for B-CDs (A), CNDs (B), Y-CDs (C), and carbon nanopowder (D).

oxygen-containing functional groups such as carboxyl (-COOH) and carbonyl (C═O) groups on the surface of B-CDs while emitting CO_2 [58,59]. Then, when temperature continues to increase from 613 to 763 °C, the mass loss is 25% with a sharp decomposition, which might be from the decomposition of oxidized sp^2 structures in the graphitic core of B-CDs [57,60]. The decomposition with a mass loss of 11% in the period of 763–1000 °C may be ascribed to presence of unoxidized sp^2 structures in the core [61]. In comparison, the TGA spectrum in Fig. 6D reveals that carbon nanopowder, the sole precursor of B-CDs, begins to decompose at an early temperature of 400 °C due to its amorphous structure, and the mass loss increases rapidly above 600 °C [62]. This thermogram bears resemblance to those previously observed for glassy carbon and carbon nanotubes and is consistent with an sp^2 carbon structure [61,63,64]. The mass percentage lower than 0% in Fig. 6D is caused by systematic instrumentation errors. A qualitative analysis of the hypothesized structures provides some information regarding the masses of each group in B-CDs. Table S3 shows the mean surface composition of B-CDs according to the mass loss over time. A comparison of these values and the ratios obtained from XPS shows an approximate similarity.

The TGA measurement of CNDs in Fig. 6B also exhibits five decomposition stages. For better demonstration of each decomposition stage and its corresponding structure, TGA was also separately performed on the precursors of CNDs, namely citric acid and urea. For the decomposition of CNDs, the first stage (40–168 °C) shows a slight mass loss (11%) caused by the evaporation of water molecules adsorbed on CNDs or formed in dehydration reactions [56,57]. Considering that urea is one of the precursors of CNDs, the mass loss might be also ascribed to the formation of ammonia gas [65]. Then the second stage (168–338 °C) and the third stage (338–448 °C) each reveal a mass loss of 18%. With the TGA of B-CDs as a reference, the decomposition of CNDs in the temperature range of 168–448 °C is due to the presence of oxygen-containing functional groups such as C═O and –COOH [58,59]. In contrast, the fourth stage (448–618 °C) exhibits an appreciably larger mass loss of 40%. This could be due to a nitrogen doped carbon lattice which decomposes at lower temperatures than the pure sp^2 carbon lattices of B-CDs due to the introduction of structural defects through heteroatom doping [66,67]. The last stage ranging between 618 and 688 °C might be ascribed to the decomposition of the s-triazine moiety [68,69]. Table S4 shows the approximate composition of CNDs according to the mass loss over time.

The thermogram of Y-CDs displays four decomposition stages in Fig. 6C. The first stage for the Y-CDs decomposition at 40–203 °C is due to the evaporation of water adsorbed on Y-CDs or generated through dehydration reactions [56,57]. This mass loss might be also ascribed to the formation of ammonia gas due the presence of $-NH_2$ groups [65]. The mass loss (27%) during the second and third stages from 203 to 433 °C is due to the decomposition of C═O and/or –COOH. The fourth stage from 433 to 658 °C corresponds to the decomposition of sp^3 carbon or other organic-like structures in the cores of Y-CDs. Table S5 approximates the mean composition of Y-CDs according to the mass loss with increasing temperature.

The TGA graphs for the precursors of CNDs and Y-CDs are presented in Fig. S11. The previously discussed thermograms of CNDs and Y-CDs display significant deviation from their precursors as is expected considering the changes which occur in the CDs' preparation process. Of these three CDs, Y-CDs present the least thermostable structure of the CDs studied, which corroborates the evidence from Raman spectroscopy and mere appearance that they are the least graphitized. For all three CDs samples tested more data is needed to identify or confirm their structures, particularly for the core.

3.2.2. Core structure

Among the techniques used in this study, X-ray diffraction/scattering appears to be only one which provides information exclusively on the core of CDs. This is vital since it is often difficult to distinguish between the signals coming from core and surface with other techniques. First inspection of the XRD pattern for each

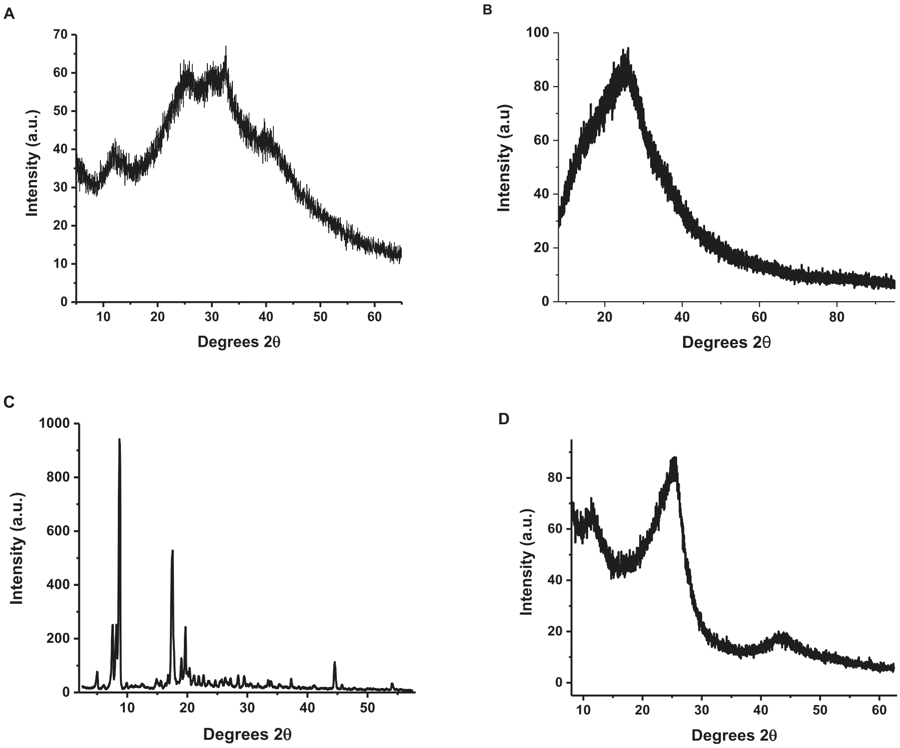

Fig. 7. XRD patterns for B-CDs (A), CNDs (B), Y-CDs (C), and carbon nanopowder (D).

CDs immediately shows that Y-CDs possesses a dramatically different core (Fig. 7). Based on this intensity and sharpness of the peaks we can say that Y-CDs possess a much higher degree of crystallinity than the amorphous B-CDs, CNDs, or B-CDs' precursor, carbon nanopowder.

To begin the closer inspection of this data, we will focus on the carbon nanopowder since it is pure carbon and can inform the analysis of B-CDs. From this spectrum (Fig. 7D), there are 3 peaks observed at 12, 25, and 43° corresponding to d-spacings of 0.74, 0.36, and 0.23 nm, respectively. The latter two peaks exhibit a great deal of similarity with the XRD pattern for glassy carbon and overall this pattern agrees with what is known for turbostratic carbon [55,70]. The peak at 25° shows a slightly larger d-spacing than the 002 plane in graphite which could indicate the presence of a nonideally arranged graphite-like structure [71]. The peak at 43° is also present in some graphite samples indicating a 100 plane [72]. The third peak from the carbon nanopowder is at 12° potentially arising from the 004 plane of graphite. This also shares similarity with peaks observed for fullerene and single-wall carbon nanotubes as it indicates the size of the fullerene cage (0.72 nm) or the diameter of the nanotube [73,74].

The XRD pattern for B-CDs possesses the same broad shape indicative of an amorphous structure, but it also possesses more peaks. The peaks at 12 and 25° are retained from the carbon nanopowder, but there is also a new peak at 32°, and the last peak has shifted to a slightly shorter angle than seen for the precursor at 40°. The changes from the carbon nanopowder are most likely due to the distortion of the lattices as they are broken off into the small, spherical B-CDs. The new peak at 32° may be due to the distortion of the 002 and 100 graphitic-like planes from the precursor, or it could arise from the small, circular structure generated in the reaction as similar peaks have been observed in the XRD pattern of carbon nanotubes [74]. The peaks at longer angles could also result from binding between lattices effectively reducing the d-spacing [75]. This could be through carbonyl or, more likely, epoxide linkages between lattices. The peak at 12° may come from the 004 plane of graphite or also include lattices with an oxidized face which increases the lattice spacing to account for the oxygen containing groups [75,76]. The array of peaks from the XRD pattern indicates that B-CDs are not simply a type of graphene quantum dots which typically possesses only the peak around 27° [77].

CNDs exhibit the simplest XRD pattern of the samples tested in this work (Fig. 7B). The weak, broad peak once again indicates an amorphous structure as observed for B-CDs. In contrast, only one peak is observed at 25° corresponding to a lattice spacing of 0.36 nm. Planar carbon nitride has been reported with a peak in the XRD pattern at 27° showing a spacing of 0.34 nm [78]. The increase in spacing here is plausibly due to the small particle size seen in CNDs as compared to the larger, planar structure of graphitic carbon nitride. The composition of the lattices is certainly more complex than B-CDs' lattices considering the bottom-up approach, but the spacing is more uniform.

Y-CDs possesses the most complex XRD pattern (Fig. 7C). The crystallinity of Y-CDs is immediately apparent from the sharp narrow peaks in comparison to the amorphous structures of the other 3 XRD patterns. The large number of peaks observed in this pattern, at least 45 with signal to noise greater than 3, indicates a polycrystalline sample. The most intense peak occurs at a 2θ value of 8.8° corresponding to a d-spacing of 1.01 nm and the second most intense is different by a factor of 2 at 17.5° corresponding to 0.51 nm. This indicates that the most important spacings are not randomly determined but may be due to a linker between the lattices. The presence of so many small peaks indicates that there are a lot of minor variation potentially resulting in similar but distinct structures. Similar XRD patterns have been observed for metal organic frameworks (MOFs) [79]. While there is no coordinate metal for Y-CDs, covalent organic frameworks (COFs) are known to display this type of crystallinity as well [80]. This comparison is an important consideration when thinking of Y-CDs structure.

SAXS confirms the results observed from XRD (Fig. S12). The carbon nanopowder and CNDs show no signal above background (data not shown) confirming their amorphous nature. For B-CDs there appears to be a small peak at 12°, but otherwise there is not a peak seen above the background, again indicating an amorphous structure. Y-CDs' SAXS pattern shares many similarities with the XRD pattern. Not as many peaks are observed, most likely due to the strong background of the Kapton tape obscuring some of them. Peak positions are similar with minor differences attributable to instrument variation. Overall, SAXS confirms what is observed from XRD.

4. Potential pathways of formation

Before discussing the structural model for each CDs, it is important to examine their possible mechanisms of formation. These reaction pathways are summarized in Fig. 8 and are reasonable possibilities for the reactions which begin the preparation process of CDs. B-CDs represent a top-down approach, so the bulk structure of the precursor is not changed much, but small particles from the edges of the nanopowder, or turbostratic, graphitic particles embedded in the larger carbon structure, are broken off in the oxidation process which creates small particles and produces a highly oxidized surface of epoxides, carboxylic acids, and alcohols (Fig. 8A). Note that the black circles representing carbon nanopowder and B-CDs in Fig. 8A are not drawn to scale. Specific structural details will be discussed in the next section.

CNDs showed the most complex array of potential reaction pathways (Fig. 8B). In the first synthetic stage, urea reacted with citric acid producing the amide derivative (5). This can further evolve under microwave irradiation with the formation of dimers connected head-to-tail (12), head-to-center (6) and center-to-center (19). Both (12) and (6) could easily evolved to complex cyclic structures through intramolecular cyclization process. Similarly, (19) could lead to the formation of (22) but this pathway was far less relevant due to the high steric hindrance barrier in the formation of (19). All the intermediates of the tree pathways could further react with each other forming complex structure characterized by amine, amide and carboxylic functionalities together with aromatic moieties. After evaporation of water in the microwave reaction, these structures which formed in the process of overnight stirring and in the first minutes of the microwave reaction undergo carbonization to form small 2D structures of varying composition and aromaticity (in contrast to the sp^2 carbon lattices of B-CDs).

For Y-CDs, there is not enough energy to induce carbonization (supported by the non-carbonized physical appearance) so the core formation is an important consideration. Some possible reactions leading to the formation of Y-CDs are summarized in Fig. 8C. Citric acid can react with *o*-PDA to initially form amide derivatives followed by the formation of polymeric structures (1). Additionally, amine groups of *o*-PDA can react with two citric acid

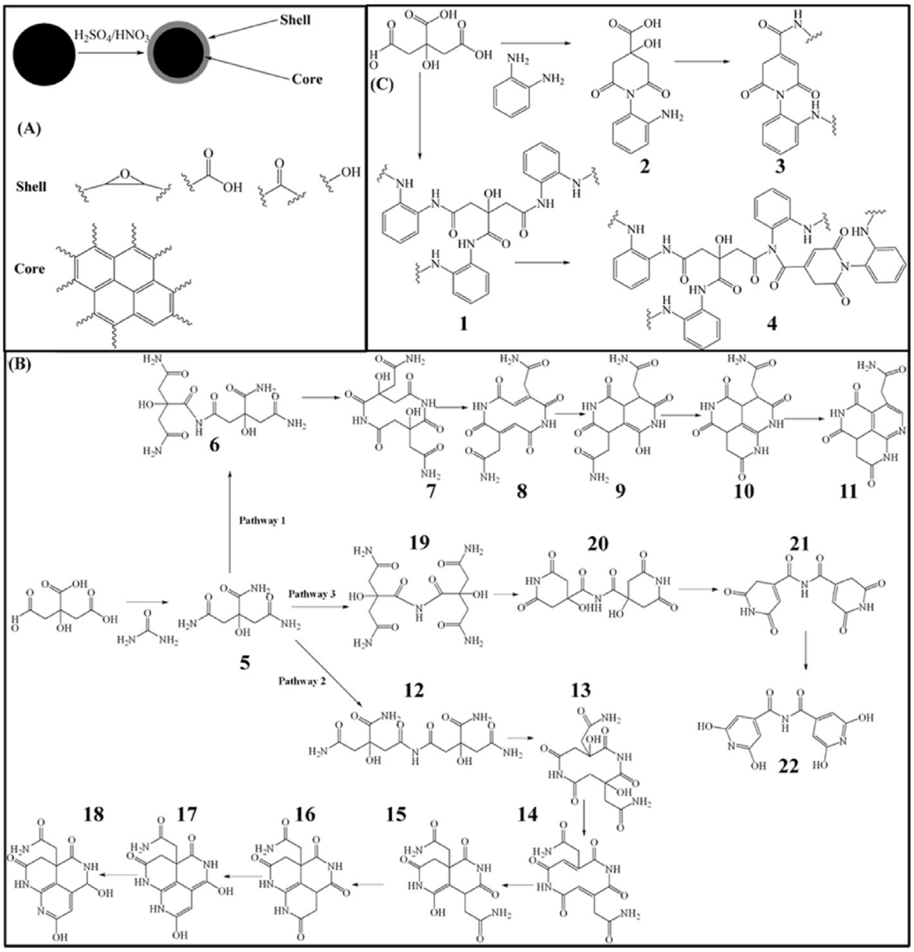

Fig. 8. Main chemical pathways involved in the assembling of B-CDs (A), CNDs (B), Y-CDs(C).

carboxylic functionalities with the formation of cyclic unsaturated amine (2,3) functionalized on nitrogen atom with a *o*-PDA residue and a carboxylic functionality. This can react with citric acid and introduce a new complex sub-structure (4). Also, the oligomerization of the *o*-PDA may proceed in a linear or branched fashion (Fig. S14). Considering the lack of a strong oxidant/energy source for this reaction, we expect that these oligomers would be more branched in nature. These three reactions occur to form polymers which possess more rigid sections (linear *o*-PDA oligomerization, citric acid heterocycle formation) and more flexible regions (branched *o*-PDA oligomerization, citric acid/*o*-PDA bound through peptide bond) which can arrange in three dimensions through a complex network of bonds and interactions ranging from amides, hydrogen bonds, and π-π stacking interaction to form Y-CDs as discussed in section 5. These reactions help to explain the negative Zeta potential as the reactions in Fig. 8 are mostly a 1:1 or low ratio between citric acid and *o*-PDA which will produce more oxygen containing groups than amines in the product as citric acid has a high oxygen content. Additionally, the oligomerization of *o*-PDA would consume only amine groups, again leaving behind more free oxygen groups which can reduce the value for Zeta potential.

The great variety of species hypothesized found a partial confirmation considering the FTIR spectra that support for example the presence of nitrogen atoms inserted into aromatic rings of CNDs (Figs. 8B, 11 and 18, 22), free amine due to *o*-PDA amine unreacted groups in Y-CD (Fig. 8C) and oxygenated carbon in B-CDs (Fig. 8A).

5. Proposed model

We will begin by examining B-CDs. In addition to the previously discussed data, we have also previously reported that B-CDs possess 5.80×10^{-3} mol –COOH/g as measured through titration [81]. This titration was performed with a standard NaOH solution and the endpoint was indicated through use of phenolphthalein, assuming –COOH was the dominant acidic group available on the surface of CDs. Beginning from this point we can perform a simple calculation on this system summarized in Fig. S13. Using Avogadro's number, a value of 3.49×10^{21} –COOH groups/g can be calculated. To convert to moles, we need a mass for B-CDs which can be obtained by subtraction of the mass of transferrin (80,000 Da) and B-CDs conjugated to transferrin obtained from a MALDI mass spectrometer. These values have been averaged to provide a value of 3650 g/mol [30,35,81,82]. Using this mass value, a value of 1.27×10^{25} –COOH groups/mol is calculated. Again, using Avogadro's number, we can convert this value in moles to particles and we obtain a value of 21.1 –COOH groups/particle. Here we need to introduce values from XPS, and we assume that this technique is able to see the entirety of the particle and the data is representative of the composition of the ensemble of particles. Using XPS values it is calculated that there is 70.9 -C-O/-C=O groups/particle and, by extension, 113.4 oxygen atoms/particle. This value can be related to the amount of carbon to give 141.4 carbon atoms/particle. Using the respective atomic masses, a particular mass of 3511 g/mol can be calculated. This is 139 g/mol or 3.8% off of our measured mass of 3650 g/mol. This deviation can be attributed to representing a range of particles with average values or to the likelihood that we are seeing a bias to the surface from XPS data.

With this calculation in hand, all our data must be reviewed to create a model. To summarize, we expect B-CDs possesses a core of mostly sp^2 carbon, surface groups of –COOH, –OH, and C=O, lattice d-spacings of 0.74, 0.36, 0.29, and 0.25 nm, a disordered, non-crystalline structure, and a molecular weight just above 3500 Da. These elements are all combined in the model displayed in Fig. 9.

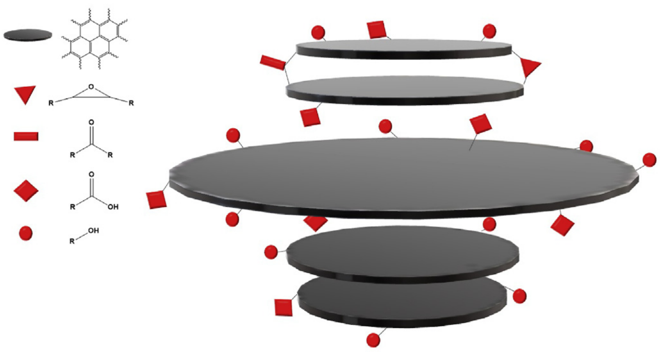

Fig. 9. Hypothesized structural model of B-CDs.

The key to this model comes from understanding the oxidation of graphite [75,76]. The lattice spacing giving rise to 0.36 nm is dominant in the XRD pattern of carbon nanopowder, but the other peaks develop or are more pronounced after oxidation. Li et al. showed the potential of oxidants, H_2SO_4 particularly, to intercalate between the carbon lattices and oxidize the interior of a carbon structure [75]. By introducing the resulting functional groups, the d-spacing of the lattices is dramatically increased, giving rise to the 0.74 nm d-spacing seen for B-CDs. The oxidation of the edge of these lattices creates highly reactive radicals which can form C–O–C bonds between lattices [76]. This more tightly bound system would be responsible for the lower d-spacings of 0.25 and 0.29 nm, depending on the degree of binding. These could also be related to the more minor graphitic planes. The presence of epoxide groups may help to explain the unusual bone targeting properties of B-CDs as the epoxide is well known for binding to collagen [24,83–85]. This model is compatible with the TGA data for B-CDs, as it shows decompositions at lower temperatures arising from the oxidized surface, intermediate temperatures coming from the lattices with interior oxidation, and finally at high temperatures from the segments of the core which are pure carbon. The model is about 2 nm in diameter and also displays all appropriate surface functionalization which we would expect based on FTIR, XPS, and Zeta potential. It should be noted that there are far more oxygen atoms on the surface of the particle, but just representative groups have been shown in Fig. 9 for clarity. This model is slightly smaller than the average particle for B-CDs as seen from TEM (3 nm), but smaller and larger particles can easily be accounted for by increased layers of sp^2 carbon and/or large lattice sizes.

For CNDs, the picture is slightly more complex since it is not possible to obtain all data for CNDs that was used for B-CDs. For

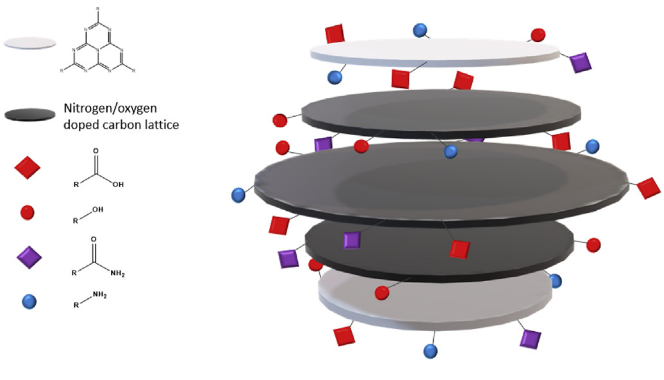

Fig. 10. Hypothesized structural model of CNDs. (A colour version of this figure can be viewed online.)

example, the measurement of –COOH groups was not possible by titration due to the more complex and varied surface groups. The data used for this model can be summarized as follows: the core should be a combination of carbon, oxygen, and nitrogen; various surface groups are present as indicated by FTIR/XPS, a lattice spacing of 0.36 nm is indicated, and the structure should possess more order than B-CDs. Additionally, it is believed that there is an s-triazine component of the structure based on FTIR and ^{13}C NMR [31]. Based on this, the model in Fig. 10 was developed. In terms of lattice types there should be 2 main types: nitrogen-doped sp^2 carbon lattices (from citric acid and urea, dark gray disks) and low molecular weight s-triazine structures (from urea alone, light gray disks), which may be randomly present in the sample. The former is formed by polymerization among the precursors followed by carbonization in the microwave. The lack of interior oxidation and lattice linkages provides the single lattice spacing observed which is somewhat similar to graphitic carbon nitride. This single spacing provides the more ordered structure expected and which is disrupted in the area with a detectable Raman signal by the presence of the C–N triple bond. Like the B-CDs model, this structure is also around 2 nm in diameter (similar to mean size seen from TEM) and only shows representative surface groups.

For Y-CDs, much of the data suggests a different type of structure than B-CDs or CNDs. The structural characterization points toward a unique model, which is expected considering the optical properties are mostly distinct from B-CDs and CNDs as well. For Y-CDs, we expect a core with a crystalline and highly ordered structure and the model should accommodate multiple lattice spacings. Y-CDs also possess lower thermostability and the groups indicated by FTIR/XPS. Additionally, the oligomerization of *o*-PDA must be considered. Previous work has been done to prepare microparticles from the oxidation of *o*-PDA and the polymerization in these cases is believed to be mostly linear (Fig. S14) [86,87]. The driving force in these reactions included strong oxidants and harsh reactions conditions leading to the thermodynamically stable linear structure. For the reaction for Y-CDs, only a mild oxidant is present, and the method is simply ultrasonication so these conditions should lead to the more kinetically controlled branched structure in Fig. S14.

Considering these elements, the model in Fig. 11 was developed. It is believed that the branched polymer can fold on itself depending on the rigidity of different sections of the polymer. The C–N single bond between benzyl units and the aliphatic structure of citric acid allows the rotation of the polymer to form these small 3D structures. The main spacings indicated by XRD are accounted for by different spacing units of the polymer (Fig. S15). Minor variations on these linkages between the layers leads to the large amount of XRD peaks. Polymers typically do not have crystal structures, but examples where they do have been reported before [88–92]. The crystallinity of any polymer is related to the order of the structure as syndiotactic and isotactic polymers are known to favor higher crystallinity [93,94]. Several data sets (absorbance, Raman, ESR, and XRD) point toward this ordered, crystalline structure, which may suggest that the oligomerization of *o*-PDA may be the dominant reaction pathway as this would favor a more ordered structure. As previously mentioned, COFs also display this crystallinity, which may indicate the type of 2D/3D structure formation that occurs for Y-CDs. This structure not only accounts for the crystallinity and order of the Y-CDs, but also the lower thermostability as this more organic structure would be less stable than the lattice structure for B-CDs and CNDs. Additionally, the hydrophobic core accounts for the amphiphilicity of Y-CDs and explains the significant changes in the optical properties in solvents of varying polarity [33]. Again, this particle would be approximately 2 nm which is the measured size determined from TEM.

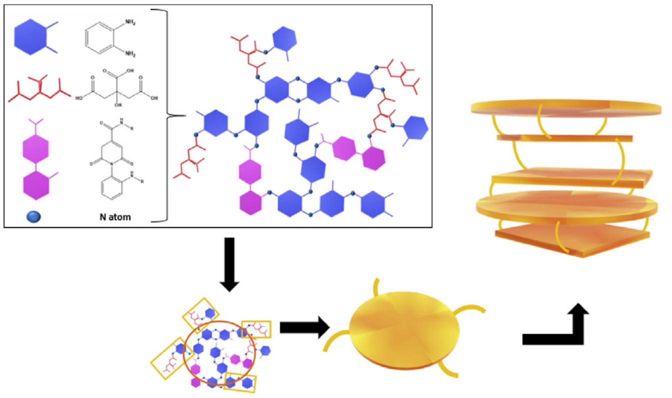

Fig. 11. Hypothesized structural model of Y-CDs. (A colour version of this figure can be viewed online.)

The structures for B-CDs and CNDs share some similarities with previous reports for CDs. Many CDs are thought to rely on the sp^2 lattice proposed in this work and some of these works have been excellently reviewed by Yang and coworkers [95,96]. There is also dissimilarities with previous results as there is no evidence for a diamond-like or sp^2/sp^3 structure being a major factor for B-CDs and CNDs. Several computational studies have shown that sp^2 "islands" or subdomains in CDs structure are present and begin to account for some of their interesting properties [97,98]. In the case of B-CDs, these subdomains may be determined by defects in the lattice through atom occlusion or an interrupting sp^3 atom. For CNDs, atom occlusion and heteroatom doping may help to determine sp^2 subdomains. The structure of Y-CDs appears to possess much more unique elements than the other two particles. While polymeric structures have been suggested for CDs, there is, to our knowledge, only one other example which shows the degree of crystallinity seen for Y-CDs, which unsurprisingly uses PDA as a precursor [99]. It is important, moving forward, to compel detailed structural characterization for reported CDs in order to compare the resulting structures from various preparation methods.

6. Conclusion

The vigorous structural characterization of CDs necessary to develop the structural models essential for the future of this material is currently lacking in research literature. This work endeavors to begin filling this gap. The optical and structural properties of three CDs has been rigorously analyzed. While the optical properties of these CDs have been previously reported, herein contains a comparative analysis. The absorption data obtained was used to measure the order of each CDs system and the degree of order obtained (Y-CDs > CNDs > B-CDs) agrees with further structural characterization. The use of Raman and ESR spectroscopies and XRD showed the presence of a disordered, amorphous structure for B-CDs and CNDs and an ordered, crystalline structure for Y-CDs. The combination of this data with XPS, FTIR, TGA, mass, titration, and AFM/TEM allowed well-defined, feasible structural models to be developed (Figs. 9–11). As has been previously mentioned, there is undoubtedly a distribution of structures in each sample, however each model stands as a representative structure. Future work would concern the computational modeling of the structures to examine their likelihood to produce the observed optical properties. This would not only help to validate the hypothesized structures but provide future opportunities to rationally design and improve CDs' properties. The greater understanding of CDs' structure obtained in this paper and through future work will improve the applications of CDs in nanomedicine by allowing a detailed investigation and understanding of their toxicological properties and enabling improvement of their surface and PL properties to optimize delivery and imaging applications.

CRediT authorship contribution statement

Keenan J. Mintz: Conceptualization, Methodology, Validation, Formal analysis, Investigation, Data curation, Writing - original draft, Writing - review & editing, Visualization. **Mattia Bartoli:** Conceptualization, Validation, Formal analysis, Investigation, Data curation, Writing - original draft, Writing - review & editing. **Massimo Rovere:** Conceptualization, Validation, Formal analysis. **Yiqun Zhou:** Methodology, Formal analysis, Investigation, Data curation, Writing - review & editing. **Sajini D. Hettiarachchi:** Methodology, Investigation. **Suraj Paudyal:** Formal analysis, Investigation. **Jiuyan Chen:** Investigation, Data curation. **Justin B. Domena:** Formal analysis, Investigation. **Piumi Y. Liyanage:** Methodology, Investigation. **Rachel Sampson:** Methodology, Investigation. **Durga Khadka:** Investigation, Data curation. **Raja R. Pandey:** Investigation, Formal analysis, Data curation. **Sunxiang Huang:** Investigation, Formal analysis, Supervision. **Charles C. Chusuei:** Investigation, Formal analysis, Data curation, Supervision. **Alberto Tagliaferro:** Conceptualization, Validation, Formal analysis, Data curation, Writing - original draft, Writing - review & editing, Supervision. **Roger M. Leblanc:** Conceptualization, Validation, Formal analysis, Writing - review & editing, Supervision, Funding acquisition.

Declaration of competing interest

The authors declare that they have no known competing financial interests or personal relationships that could have appeared to influence the work reported in this paper.

Acknowledgement

R.M.L. would like to acknowledge the financial support of the National Science Foundation through awards #1809060 and #2041413.

Appendix A. Supplementary data

Supplementary data to this article can be found online at https://doi.org/10.1016/j.carbon.2020.11.017.

References

[1] J.E. Riggs, Z. Guo, D.L. Carroll, Y.-P. Sun, Strong luminescence of solubilized carbon nanotubes, J. Am. Chem. Soc. 122 (24) (2000) 5879–5880.
[2] X. Xu, R. Ray, Y. Gu, H.J. Ploehn, L. Gearheart, K. Raker, W.A. Scrivens, Electrophoretic analysis and purification of fluorescent single-walled carbon nanotube fragments, J. Am. Chem. Soc. 126 (40) (2004) 12736–12737.
[3] Y.-P. Sun, B. Zhou, Y. Lin, W. Wang, K.S. Fernando, P. Pathak, M.J. Meziani, B.A. Harruff, X. Wang, H. Wang, Quantum-sized carbon dots for bright and colorful photoluminescence, J. Am. Chem. Soc. 128 (24) (2006) 7756–7757.
[4] J. Wang, J. Qiu, A review of carbon dots in biological applications, J. Mater. Sci. 51 (10) (2016) 4728–4738.
[5] K.J. Mintz, G. Mercado, Y. Zhou, Y. Ji, S.D. Hettiarachchi, P.Y. Liyanage, R.R. Pandey, C.C. Chusuei, J. Dallman, R.M. Leblanc, Tryptophan carbon dots and their ability to cross the blood-brain barrier, Colloids Surf. B Biointerfaces 176 (2019) 488–493.
[6] Y. Zhou, E.M. Zahran, B.A. Quiroga, J. Perez, K.J. Mintz, Z. Peng, P.Y. Liyanage, R.R. Pandey, C.C. Chusuei, R.M. Leblanc, Size-dependent photocatalytic activity of carbon dots with surface-state determined photoluminescence, Appl. Catal. B Environ. 248 (2019) 157–166.
[7] X. Sun, Y. Lei, Fluorescent carbon dots and their sensing applications, Trends Anal. Chem. 89 (2017) 163–180.
[8] S. Zhu, Y. Song, X. Zhao, J. Shao, J. Zhang, B. Yang, The photoluminescence mechanism in carbon dots (graphene quantum dots, carbon nanodots, and polymer dots): current state and future perspective, Nano Res. 8 (2) (2015) 355–381.
[9] K.J. Mintz, Y. Zhou, R.M. Leblanc, Recent development of carbon quantum dots regarding their optical properties, photoluminescence mechanism, and core structure, Nanoscale 11 (11) (2019) 4634–4652.
[10] M.K. Barman, A. Patra, Current status and prospects on chemical structure driven photoluminescence behaviour of carbon dots, J. Photoch. Photobio. C 37 (2018) 1–22.
[11] J. Yeagle, Nanotechnology and the FDA, Va. JL & Tech. 12 (2007) 1–17.
[12] K. Nekoueian, M. Amiri, M. Sillanpää, F. Marken, R. Boukherroub, S. Szunerits, Carbon-based quantum particles: an electroanalytical and biomedical perspective, Chem. Soc. Rev. 48 (15) (2019) 4281–4316.
[13] F. Yan, Y. Jiang, X. Sun, Z. Bai, Y. Zhang, X. Zhou, Surface modification and chemical functionalization of carbon dots: a review, Microchim. Acta 185 (9) (2018) 424–457.
[14] P. Zuo, X. Lu, Z. Sun, Y. Guo, H. He, A review on syntheses, properties, characterization and bioanalytical applications of fluorescent carbon dots, Microchim. Acta 183 (2) (2016) 519–542.
[15] A. Kelarakis, From highly graphitic to amorphous carbon dots: a critical review, MRS Energy Sustain. 1 (E2) (2014) 1–15.
[16] V. Ansi, N. Renuka, Exfoliated graphitic carbon dots: application in heavy metal ion sensing, J. Lumin. 205 (2019) 467–474.
[17] B.C. Martindale, G.A. Hutton, C.A. Caputo, S. Prantl, R. Godin, J.R. Durrant, E. Reisner, Enhancing light absorption and charge transfer efficiency in carbon dots through graphitization and core nitrogen doping, Angew. Chem. Int. Ed. 56 (23) (2017) 6459–6463.
[18] S. Wei, X. Yin, H. Li, X. Du, L. Zhang, Q. Yang, R. Yang, Multi-color fluorescent carbon dots: non-size effect dominate graphitized sp2 conjugated domain and surface state energy level co-modulate band-gap, Chem. Eur J. 26 (2020) 8129–8136.
[19] N.V. Tepliakov, E.V. Kundelev, P.D. Khavlyuk, Y. Xiong, M.Y. Leonov, W. Zhu, A.V. Baranov, A.V. Fedorov, A.L. Rogach, I.D. Rukhlenko, sp2–sp3-Hybridized atomic domains determine optical features of carbon dots, ACS Nano 13 (9) (2019) 10737–10744.
[20] Q. Xu, W. Cai, M. Zhang, R. Su, Y. Ye, Y. Li, L. Zhang, Y. Guo, Z. Yu, S. Li, Photoluminescence mechanism and applications of Zn-doped carbon dots, RSC Adv. 8 (31) (2018) 17254–17262.
[21] F. Pschunder, M.A. Huergo, J.M. Ramallo-Lopez, B. Kommula, F.G. Requejo, S. Bhattacharyya, Role of intrinsic atomic Features and bonding motifs from the surface to the deep core on multistate emissive properties of N, B-co doped carbon dots, J. Phys. Chem. C 124 (2020) 1121–1128.
[22] L. Li, T. Dong, Photoluminescence tuning in carbon dots: surface passivation or/and functionalization, heteroatom doping, J. Mater. Chem. C 6 (30) (2018) 7944–7970.
[23] K. Hola, M. Sudolska, S. Kalytchuk, D. Nachtigallova, A.L. Rogach, M. Otyepka, R. Zboril, Graphitic nitrogen triggers red fluorescence in carbon dots, ACS Nano 11 (12) (2017) 12402–12410.
[24] Z. Peng, E.H. Miyanji, Y. Zhou, J. Pardo, S.D. Hettiarachchi, S. Li, P.L. Blackwelder, I. Skromne, R.M. Leblanc, Carbon dots: promising biomaterials for bone-specific imaging and drug delivery, Nanoscale 9 (44) (2017) 17533–17543.
[25] S. Sarkar, M. Sudolska, M. Dubecky, C.J. Reckmeier, A.L. Rogach, R. Zboril, M. Otyepka, Graphitic nitrogen doping in carbon dots causes red-shifted absorption, J. Phys. Chem. C 120 (2) (2016) 1303–1308.
[26] A.P. Demchenko, Excitons in carbonic nanostructures, C-J. Carbon Res. 5 (4) (2019) 71–120.
[27] E. Reisner, B. Martindale, G. Hutton, C. Caputo, S. Prantl, R. Godin, J. Durrant, Enhancing light absorption and charge transfer efficiency in carbon dots through graphitization and core nitrogen doping, Angew. Chem. Int. Ed. 129 (2017) 6559–6563.
[28] F. Zu, F. Yan, Z. Bai, J. Xu, Y. Wang, Y. Huang, X. Zhou, The quenching of the fluorescence of carbon dots: a review on mechanisms and applications, Microchim. Acta 184 (7) (2017) 1899–1914.
[29] S. Li, L. Wang, C.C. Chusuei, V.M. Suarez, P.L. Blackwelder, M. Micic, J. Orbulescu, R.M. Leblanc, Nontoxic carbon dots potently inhibit human insulin fibrillation, Chem. Mater. 27 (5) (2015) 1764–1771.
[30] S.D. Hettiarachchi, R.M. Graham, K.J. Mintz, Y. Zhou, S. Vanni, Z. Peng, R.M. Leblanc, Triple conjugated carbon dots as a nano-drug delivery model for glioblastoma brain tumors, Nanoscale 11 (13) (2019) 6192–6205.
[31] P.Y. Liyanage, R.M. Graham, R.R. Pandey, C.C. Chusuei, K.J. Mintz, Y. Zhou, J.K. Harper, W. Wu, A.H. Wikramanayake, S. Vanni, Carbon nitride dots: a selective bioimaging nanomaterial, Bioconjugate Chem. 30 (1) (2018) 111–123.
[32] P.Y. Liyanage, Y. Zhou, A.O. Al-Youbi, A.S. Bashammakh, M.S. El-Shahawi, S. Vanni, R.M. Graham, R.M. Leblanc, Pediatric glioblastoma target-specific efficient delivery of gemcitabine across the blood–brain barrier via carbon nitride dots, Nanoscale 12 (14) (2020) 7927–7938.
[33] Y. Zhou, K. Mintz, C. Oztan, S. Hettiarachchi, Z. Peng, E. Seven, P. Liyanage, S. De La Torre, E. Celik, R. Leblanc, Embedding carbon dots in superabsorbent polymers for additive manufacturing, Polymers 10 (8) (2018) 921–932.
[34] Y. Zhou, P.Y. Liyanage, D. Devadoss, L.R.R. Guevara, L. Cheng, R.M. Graham, H.S. Chand, A.O. Al-Youbi, A.S. Bashammakh, M.S. El-Shahawi, Nontoxic

amphiphilic carbon dots as promising drug nanocarriers across the blood–brain barrier and inhibitors of β-amyloid, Nanoscale 11 (46) (2019) 22387–22397.

[35] S. Li, Z. Peng, J. Dallman, J. Baker, A.M. Othman, P.L. Blackwelder, R.M. Leblanc, Crossing the blood–brain–barrier with transferrin conjugated carbon dots: a zebrafish model study, Colloids Surf. B Biointerfaces 145 (2016) 251–256.

[36] Y. Zhou, P.Y. Liyanage, D.L. Geleroff, Z. Peng, K.J. Mintz, S.D. Hettiarachchi, R.R. Pandey, C.C. Chusuei, P.L. Blackwelder, R.M. Leblanc, Photoluminescent carbon dots: a mixture of heterogeneous fractions, ChemPhysChem 19 (19) (2018) 2589–2597.

[37] H. Ding, S.-B. Yu, J.-S. Wei, H.-M. Xiong, Full-color light-emitting carbon dots with a surface-state-controlled luminescence mechanism, ACS Nano 10 (1) (2015) 484–491.

[38] A. Philippidis, A. Spyros, D. Anglos, A.B. Bourlinos, R. Zbořil, E.P. Giannelis, Carbon-dot organic surface modifier analysis by solution-state NMR spectroscopy, J. Nano Res. 15 (7) (2013) 1777–1785.

[39] M.L. Liu, B.B. Chen, C.M. Li, C.Z. Huang, Carbon dots: synthesis, formation mechanism, fluorescence origin and sensing applications, Green Chem. 21 (2019) 449–471.

[40] A.C. Vandaele, C. Hermans, P.C. Simon, M. Van Roozendael, J.M. Guilmot, M. Carleer, R. Colin, Fourier transform measurement of NO_2 absorption cross-section in the visible range at room temperature, J. Atmos. Chem. 25 (3) (1996) 289–305.

[41] M. Merienne, A. Jenouvrier, B. Coquart, The NO_2 absorption spectrum. I: absorption cross-sections at ambient temperature in the 300–500 nm region, J. Atmos. Chem. 20 (3) (1995) 281–297.

[42] D. Dasgupta, F. Demichelis, C. Pirri, A. Tagliaferro, π bands and gap states from optical absorption and electron-spin-resonance studies on amorphous carbon and amorphous hydrogenated carbon films, Phys. Rev. B 43 (3) (1991) 2131–2135.

[43] G. Fanchini, S. Ray, A. Tagliaferro, Density of electronic states in amorphous carbons, Diam. Relat. Mater. 12 (3–7) (2003) 891–899.

[44] G. Fanchini, A. Tagliaferro, Localisation and density of states in amorphous carbon-based alloys, Diam. Relat. Mater. 10 (2) (2001) 191–199.

[45] X. Liu, Z. Xu, J.M. Cole, Molecular design of UV–vis absorption and emission properties in organic fluorophores: toward larger bathochromic shifts, enhanced molar extinction coefficients, and greater Stokes shifts, J. Phys. Chem. C 117 (32) (2013) 16584–16595.

[46] J.F. Araneda, W.E. Piers, B. Heyne, M. Parvez, R. McDonald, High Stokes shift anilido-pyridine boron difluoride dyes, Angew. Chem. Int. Ed. 50 (51) (2011) 12214–12217.

[47] P. Namdari, B. Negahdari, A. Eatemadi, Synthesis, properties and biomedical applications of carbon-based quantum dots: an updated review, Biomed. Pharmacother. 87 (2017) 209–222.

[48] J. Zhou, H. Zhou, J. Tang, S. Deng, F. Yan, W. Li, M. Qu, Carbon dots doped with heteroatoms for fluorescent bioimaging: a review, Microchim. Acta 184 (2) (2017) 343–368.

[49] N.K. Bhardwaj, V. Hoang, K.L. Nguyen, Effect of refining on pulp surface charge accessible to polydadmac and FTIR characteristic bands of high yield kraft fibres, Bioresour. Technol. 98 (4) (2007) 962–966.

[50] S.D. Gardner, C.S. Singamsetty, G.L. Booth, G.-R. He, C.U. Pittman, Surface characterization of carbon fibers using angle-resolved XPS and ISS, Carbon 33 (5) (1995) 587–595.

[51] U. Olgun, M. Gülfen, Doping of poly (*o*-phenylenediamine): spectroscopy, voltammetry, conductivity and band gap energy, React. Funct. Polym. 77 (2014) 23–29.

[52] S. Mentus, G. Ćirić-Marjanović, M. Trchova, J. Stejskal, Conducting carbonized polyaniline nanotubes, Nanotechnology 20 (24) (2009) 245601–245610.

[53] P. Sett, A. De, S. Chattopadhyay, P. Mallick, Raman excitation profile of diphenylamine, Chem. Phys. 276 (2) (2002) 211–224.

[54] M. Takahashi, M. Goto, M. Ito, Surface-enhanced Raman scattering of phenazine. Large intensities of overtones and combination bands, Chem. Phys. Lett. 121 (4–5) (1985) 458–463.

[55] S. Bukalov, L. Leites, A. Sorokin, A. Kotosonov, Structural changes in industrial glassy carbon as a function of heat treatment temperature according to Raman spectroscopy and X-Ray diffraction data, Nanosyst.: Phys. Chem. Math. 5 (2014) 186–191.

[56] G. Huang, X. Chen, C. Wang, H. Zheng, Z. Huang, D. Chen, H. Xie, Photoluminescent carbon dots derived from sugarcane molasses: synthesis, properties, and applications, RSC Adv. 7 (75) (2017) 47840–47847.

[57] A. Mewada, S. Pandey, M. Thakur, D. Jadhav, M. Sharon, Swarming carbon dots for folic acid mediated delivery of doxorubicin and biological imaging, J. Mater. Chem. B 2 (6) (2014) 698–705.

[58] D. Wang, Z. Wang, Q. Zhan, Y. Pu, J.-X. Wang, N.R. Foster, L. Dai, Facile and scalable preparation of fluorescent carbon dots for multifunctional applications, Engineering 3 (3) (2017) 402–408.

[59] A. Mewada, S. Pandey, S. Shinde, N. Mishra, G. Oza, M. Thakur, M. Sharon, M. Sharon, Green synthesis of biocompatible carbon dots using aqueous extract of Trapa bispinosa peel, Mater. Sci. Eng. C 33 (5) (2013) 2914–2917.

[60] L.M. Viculis, J.J. Mack, O.M. Mayer, H.T. Hahn, R.B. Kaner, Intercalation and exfoliation routes to graphite nanoplatelets, J. Mater. Chem. 15 (9) (2005) 974–978.

[61] D. Bom, R. Andrews, D. Jacques, J. Anthony, B. Chen, M.S. Meier, J.P. Selegue, Thermogravimetric analysis of the oxidation of multiwalled carbon nanotubes: evidence for the role of defect sites in carbon nanotube chemistry, Nano Lett. 2 (6) (2002) 615–619.

[62] Y. Zhou, K.J. Mintz, L. Cheng, J. Chen, B.C.L.B. Ferreira, S.D. Hettiarachchi, P.Y. Liyanage, E.S. Seven, N. Miloserdov, R.R. Pandey, B. Quiroga, P.L. Blackwelder, C.C. Chusuei, S. Li, Z. Peng, R.M. Leblanc, Direct conjugation of distinct carbon dots as lego-like building blocks for the assembly of versatile drug nanocarriers, J. Colloid Interface Sci. 576 (2020) 412–425.

[63] T. Durkić, A. Perić, M. Laušević, A. Dekanski, O. Nešković, M. Veljković, Z. Laušević, Boron and phosphorus doped glassy carbon: surface properties, Carbon 35 (10–11) (1997) 1567–1572.

[64] Z. Shi, Y. Lian, F. Liao, X. Zhou, Z. Gu, Y. Zhang, S. Iijima, Purification of single-wall carbon nanotubes, Solid State Commun. 112 (1) (1999) 35–37.

[65] S. Tischer, M. Börnhorst, J. Amsler, G. Schoch, O. Deutschmann, Thermodynamics and reaction mechanism of urea decomposition, Phys. Chem. Chem. Phys. 21 (30) (2019) 16785–16797.

[66] D. Bhattacharjya, H.-Y. Park, M.-S. Kim, H.-S. Choi, S.N. Inamdar, J.-S. Yu, Nitrogen-doped carbon nanoparticles by flame synthesis as anode material for rechargeable lithium-ion batteries, Langmuir 30 (1) (2014) 318–324.

[67] Y. Zhao, Z. Liu, W. Chu, L. Song, Z. Zhang, D. Yu, Y. Tian, S. Xie, L. Sun, Large-scale synthesis of nitrogen-rich carbon nitride microfibers by using graphitic carbon nitride as precursor, Adv. Mater. 20 (9) (2008) 1777–1781.

[68] R.R. Pal, P.S. Patil, M.M. Salunkhe, N.N. Maldar, P.P. Wadgaonkar, Synthesis and characterization of aromatic polyamides containing an s-triazine ring with thiophenoxy linkages, Polym. Int. 54 (3) (2005) 569–575.

[69] K. Takagi, T. Hattori, H. Kunisada, Y. Yuki, Triazine dendrimers by divergent and convergent methods, J. Polym. Sci., Polym. Chem. Ed. 38 (24) (2000) 4385–4395.

[70] T. Noda, M. Inagaki, The structure of glassy carbon, Bull. Chem. Soc. Jpn. 37 (10) (1964) 1534–1538.

[71] G. Sun, X. Li, Y. Qu, X. Wang, H. Yan, Y. Zhang, Preparation and characterization of graphite nanosheets from detonation technique, Mater. Lett. 62 (4–5) (2008) 703–706.

[72] A. Popova, Crystallographic analysis of graphite by X-Ray diffraction, Coke Chem. 60 (9) (2017) 361–365.

[73] W. Zhu, D.E. Miser, W.G. Chan, M.R. Hajaligol, Characterization of combustion fullerene soot, C60, and mixed fullerene, Carbon 42 (8–9) (2004) 1463–1471.

[74] S. Kawasaki, Y. Matsuoka, T. Yokomae, Y. Nojima, F. Okino, H. Touhara, H. Kataura, XRD and TEM study of high pressure treated single-walled carbon nanotubes and C60-peapods, Carbon 43 (1) (2005) 37–45.

[75] C. Li, X. Chen, L. Shen, N. Bao, Revisiting the oxidation of graphite: reaction mechanism, chemical stability, and structure self-regulation, ACS Omega 5 (7) (2020) 3397–3404.

[76] V. Skákalová, P. Kotrusz, M. Jergel, T. Susi, A. Mittelberger, V. Vretenár, P. Siffalovic, J. Kotakoski, J.C. Meyer, M. Hulman, Chemical oxidation of graphite: evolution of the structure and properties, J. Phys. Chem. C 122 (1) (2018) 929–935.

[77] Y. Sun, S. Wang, C. Li, P. Luo, L. Tao, Y. Wei, G. Shi, Large scale preparation of graphene quantum dots from graphite with tunable fluorescence properties, Phys. Chem. Chem. Phys. 15 (24) (2013) 9907–9913.

[78] Y. Zheng, Z. Zhang, C. Li, A comparison of graphitic carbon nitrides synthesized from different precursors through pyrolysis, J. Photochem. Photobiol., A 332 (2017) 32–44.

[79] E. Proietti, F. Jaouen, M. Lefèvre, N. Larouche, J. Tian, J. Herranz, J.-P. Dodelet, Iron-based cathode catalyst with enhanced power density in polymer electrolyte membrane fuel cells, Nat. Commun. 2 (1) (2011) 1–9.

[80] B. Lukose, A. Kuc, T. Heine, The structure of layered covalent-organic frameworks, Chem. Eur J. 17 (8) (2011) 2388–2392.

[81] Z. Peng, S. Li, X. Han, A.O. Al-Youbi, A.S. Bashammakh, M.S. El-Shahawi, R.M. Leblanc, Determination of the composition, encapsulation efficiency and loading capacity in protein drug delivery systems using circular dichroism spectroscopy, Anal. Chim. Acta 937 (2016) 113–118.

[82] S. Li, D. Amat, Z. Peng, S. Vanni, S. Raskin, G. De Angulo, A.M. Othman, R.M. Graham, R.M. Leblanc, Transferrin conjugated nontoxic carbon dots for doxorubicin delivery to target pediatric brain tumor cells, Nanoscale 8 (37) (2016) 16662–16669.

[83] E. Khor, Methods for the treatment of collagenous tissues for bioprostheses, Biomaterials 18 (2) (1997) 95–105.

[84] R. Tu, S.H. Shen, D. Lin, C. Hata, K. Thyagarajan, Y. Noishiki, R.C. Quijano, Fixation of bioprosthetic tissues with monofunctional and multifunctional polyepoxy compounds, J. Biomed. Mater. Res. 28 (6) (1994) 677–684.

[85] L.L. Huang, P. Lee, L. Chen, K. Hsieh, Comparison of epoxides on grafting collagen to polyurethane and their effects on cellular growth, J. Biomed. Mater. Res. 39 (4) (1998) 630–636.

[86] X.-G. Li, X.-L. Ma, J. Sun, M.-R. Huang, Powerful reactive sorption of silver (I) and mercury (II) onto poly (o-phenylenediamine) microparticles, Langmuir 25 (3) (2009) 1675–1684.

[87] X. Sun, S. Dong, E. Wang, Formation of *o*-phenylenediamine oligomers and their self-assembly into one-dimensional structures in aqueous medium, Macromol. Rapid Commun. 26 (18) (2005) 1504–1508.

[88] H.E. Assender, A.H. Windle, Crystallinity in poly (vinyl alcohol): an X-ray diffraction study of atactic PVOH, Polymer 39 (18) (1998) 4295–4302.

[89] H. Zhang, S. Wang, S. Zhang, R. Ma, Y. Wang, W. Cao, C. Liu, C. Shen, Crystallization behavior of poly (lactic acid) with a self-assembly aryl amide nucleating agent probed by real-time infrared spectroscopy and X-ray diffraction, Polym. Test. 64 (2017) 12–19.

[90] P. Ahvenainen, I. Kontro, K. Svedström, Comparison of sample crystallinity

determination methods by X-ray diffraction for challenging cellulose I materials, Cellulose 23 (2) (2016) 1073–1086.

[91] N. Murthy, H. Minor, General procedure for evaluating amorphous scattering and crystallinity from X-ray diffraction scans of semicrystalline polymers, Polymer 31 (6) (1990) 996–1002.

[92] Y.Z. Dong, H.J. Choi, Electrorheological characteristics of poly (diphenylamine)/magnetite composite-based suspension, Materials 12 (18) (2019) 2911–2928.

[93] F. Auriemma, C. De Rosa, A. Malafronte, M. Scoti, R. Di Girolamo, Solid state polymorphism of isotactic and syndiotactic polypropylene, in: Polypropylene Handbook, Springer, 2019, pp. 37–119.

[94] A. Bergamini, M. Miniaci, T. Delpero, D. Tallarico, B. Van Damme, G. Hannema, I. Leibacher, A. Zemp, Tacticity in chiral phononic crystals, Nat. Commun. 10 (1) (2019) 1–8.

[95] C. Xia, S. Zhu, T. Feng, M. Yang, B. Yang, Evolution and synthesis of carbon dots: from carbon dots to carbonized polymer dots, Adv. Sci. 6 (23) (2019) 1901316–1901338.

[96] M.t. Paloncýová, M. Langer, M. Otyepka, Structural dynamics of carbon dots in water and n, n-dimethylformamide probed by all-atom molecular dynamics simulations, J. Chem. Theor. Comput. 14 (4) (2018) 2076–2083.

[97] H. Yoon, Y.H. Chang, S.H. Song, E.S. Lee, S.H. Jin, C. Park, J. Lee, B.H. Kim, H.J. Kang, Y.H. Kim, Intrinsic photoluminescence emission from subdomained graphene quantum dots, Adv. Mater. 28 (26) (2016) 5255–5261.

[98] H. Chen, Y. Qiu, D. Ding, H. Lin, W. Sun, G.D. Wang, W. Huang, W. Zhang, D. Lee, G. Liu, Gadolinium-encapsulated graphene carbon nanotheranostics for imaging-guided photodynamic therapy, Adv. Mater. 30 (36) (2018) 1802748–1802756.

[99] X. Sun, C. Brückner, Y. Lei, One-pot and ultrafast synthesis of nitrogen and phosphorus co-doped carbon dots possessing bright dual wavelength fluorescence emission, Nanoscale 7 (41) (2015) 17278–17282.